Magnetic Resonance Imaging 57 (2019) 40–49

Contents lists available at ScienceDirect

Magnetic Resonance Imaging

journal homepage: www.elsevier.com/locate/mri

Original contribution

Gellan gum-based gels with tunable relaxation properties for MRI phantoms

Pawel Brzozowski[a], Kalin I. Penev[b], Francisco M. Martinez[c], Timothy J. Scholl[c,d], Kibret Mequanint[a,b,*]

[a] School of Biomedical Engineering, The University of Western Ontario, London, Canada
[b] Department of Chemical and Biochemical Engineering, The University of Western Ontario, London, Canada
[c] Department of Medical Biophysics, and the Robarts Research Institute, The University of Western Ontario, London, Canada
[d] Ontario Institute for Cancer Research, Toronto, Canada

ARTICLE INFO

Keywords:
MRI phantom
Gellan gum
SPIONs
Paramagnetic ions
Design of experiments

ABSTRACT

Object: The research follows the analysis of gellan gum-based gels as novel MRI phantom material with the implementation of a design of experiments model to obtain tunable relaxation properties.
Materials and methods: Gellan gum gels doped with newly synthesized superparamagnetic iron oxide nanoparticles (SPIONs) and either $MnCl_2$ or $GdCl_3$ were prepared and scanned from 230 μT to 3 T. Nineteen gel samples were formulated with varying concentrations of contrast agents to determine the linear, quadratic, and interactive effects of the contrast agents by a central composite design of experiment. To inhibit microbial growth in the gels and to enable long-term use, methyl 4-hydroxybenzoate (methylparaben) was utilized.
Results: The model containing SPIONs and metal salts relaxivity was analyzed with ANOVA, and the resulting significant coefficients were tabulated. The mathematical model was able to accurately predict the intended relaxation property from the concentration of the contrast agent with adjusted R^2 values > 0.97 for longitudinal (R_1) relaxation rates and 0.87 for transverse (R_2) relaxation rates.
Conclusion: The gel material maintained physical, chemical, and biological stability for at least four months and contained controllable relaxation properties while maintaining optical clarity.

1. Introduction

MRI phantoms are physical systems that provide near tissue-equivalent MRI signals typically used in calibration and ensuring consistent image quality between MRI scanners. Common requirements for an effective MRI phantom include tissue-equivalent homogenous relaxation times, ease of shaping, dimensional stability without reinforcement, simple preparation, low toxicity, and physical, chemical, and biological stability [1–3]. Typical MRI phantom materials include aqueous solutions or hydrogels doped with appropriate contrast agents [4]. Doped aqueous solutions have simple preparations, ease of use, long-term stability, and homogeneous properties, but they lack the ability to form and retain shapes, are not tissue equivalent, and are plagued with internal vibrations which, if misused, will generate imaging artifacts. By contrast, hydrogels alleviate some of these issues due to quickly diminishing internal vibrations, physical and chemical stability. Previously, synthetic and biopolymer hydrogels have been used as MRI phantoms, including PVA [5,6], gelatin [7], agar [8,9], agarose [10–12], carrageenan [2,13,14], polyacrylamide gels [15], TX-151 [16], carbomer-980 and carbopol®-974P [17], with agarose gels being the most common. However, the concentration of agarose affects the gel integrity and the relaxation properties creating structural issues when targeting specific tissues relaxation times. Additionally, agarose gels often form trapped bubbles and are either translucent or opaque due to light scattering.

In an attempt to alleviate the issues in current MRI hydrogel phantom materials, a novel gel phantom material was tested which utilized gellan gum gels as the gelling agent. Gellan gum was developed as an alternative to gelatin and agar in the food and pharmaceutical industries [18], and is an anionic polysaccharide that forms stable gels at low concentrations. Gellan gum gels can be prepared at lower temperatures than other polysaccharides, without the requirements of specialized equipment, and form bubble-free transparent or translucent gels. Compared to agarose gels, they contain a wider range of mechanical properties that are highly adjustable [19] while having reasonable thermal stability [20,21]. Although gellan gum has been used to form phantom materials that mimic the acoustic and thermal properties of human tissues [19,20,22], its utilization as an MRI phantom material has not been previously reported. With homogenous gel properties, dimensional stability, and potential compatibility with

* Corresponding author at: Department of Chemical and Biochemical Engineering, The University of Western Ontario, London, Canada.
E-mail address: kmequani@uwo.ca (K. Mequanint).

https://doi.org/10.1016/j.mri.2018.10.017
Received 8 August 2018; Received in revised form 26 October 2018; Accepted 27 October 2018

additives, gellan gum could be used as an alternative to fabricate MRI phantoms. With gellan gum gel, we expected to prepare a transparent, thermally stable, inexpensive, safe to handle, simple to prepare, and tissue equivalent MRI gel phantom.

In this manuscript, we aimed at developing gellan gum MRI phantoms containing both paramagnetic ions and superparamagnetic nanoparticles to adjust the longitudinal relaxation (T_1) and transverse relaxation (T_2) times independently, in order to mimic a wide range of human tissues. We used two paramagnetic ions (Mn^{2+} and Gd^{3+}), as manganese chloride ($MnCl_2$) and gadolinium chloride ($GdCl_3$), and superparamagnetic iron oxide nanoparticles (SPIONs) to control the relaxation properties of the gels. The use of various concentrations of metal salts and SPIONs enabled a range of relaxation times that could be used to model human tissue for a known magnetic field strength. Furthermore, we investigated the effect of temperature on the relaxation rates of the prepared gels.

2. Materials and methods

2.1. Nanoparticle preparation and characterization

SPIONs were prepared by a modified co-precipitation method using a singular iron salt [23]. Briefly, 1.4 g of iron(II) sulphate heptahydrate (Sigma Aldrich, Canada) were dissolved in 50 mL of deionized water at 40 °C for 30 min while stirring. Next, the iron salt solution was heated to 70 °C and 20 mL of 25% ammonium hydroxide (Caledon Laboratories, Canada) was added while continuously stirring with an overhead stirrer. The increased pH triggered precipitation of iron oxide particles. To ensure a complete reaction, the basic ferrous suspension was heated for 90 min at 90 °C while continuously stirring. Once complete, the mixture containing nanoparticles was cooled to room temperature before being magnetically decanted, separating the iron oxide nanoparticles from the bulk liquid. The separated iron oxide nanoparticles were purified three times by washing with 30 mL deionized water, centrifugation, and decanting. The separated SPIONs were dried under vacuum for 24 h. A suspension of SPIONs was prepared in distilled water at a concentration of 0.5 g/L and ultrasonicated before use. A Philips CM 10 transmission electron microscope (TEM) with magnification 18× to 450,000×, resolution 0.5 nm (point) or 0.34 nm (line), and voltage 40 kV to 100 kV was used to determine morphology and size of the SPIONs. The size distribution was determined by estimating the diameters of 421 particles using ImageJ. X-ray Diffraction (XRD) (MiniFlex-Rigaku, The Woodlands, TX) analysis investigated the crystallite structure and the crystalline size (at 2-theta from 20 to 70° at 0.02 step size, 40 kV X-ray). From the XRD the average crystallite size was estimated by the Scherrer equation:

$$D_p = \frac{0.94\lambda}{\beta_{1/2}\cos\theta} \quad (1)$$

where D_p represents the average crystallite size, $\beta_{1/2}$ represents the line broadening in radians or the full width half maximum, θ represents the Bragg angle, and λ represents the X-ray wavelength. The magnetic properties of the dried SPIONs were analyzed with a vibrating sample magnetometer (VSM 7407) (Lake Shore cyrotonics, Westerville, OH). The dried powdered SPIONs were characterized at moment measure range of 10^{-10} to 1 J/T (10^{-7} to 10^{3} emu) at room temperature and up to a maximum field of 1 T (10 kOe). The saturation magnetism, coercivity, and retentivity were determined and compared to literature values.

2.2. Gellan gum gel preparation

Gellan gum gels were prepared similar to our published procedure [24]. As gellan gum is susceptible to bacterial growth, methyl 4-hydroxybenzoate (methylparaben) and propylene glycol were utilized as preservatives instead of the more common sodium azide which is undesirable due to its human toxicity [25]. Methyl 4-hydroxybenzoate is an antiseptic used in pharmaceuticals, and a preservative in the food industry [26] and propylene glycol also exhibits antibacterial properties [27] while aiding in the homogeneity and stability of the gel. To prepare the gels (per 100 mL): 1.25 g gellan gum powder (Alfa Aesar, USA) and 100 mg methyl 4-hydroxybenzoate (Sigma Aldrich, Canada) were added into 10.0 mL propylene glycol (Caledon Laboratories, Canada) to solvate the powders. Deionized water (52.5 mL) was then added with vigorous mixing at room temperature in order to disperse the powder. The resulting suspension was heated until complete dissolution. The transparent gel solution was cooled to 55 °C and mixed with the SPION solution and the metal salt solutions of gadolinium(III) chloride hexahydrate ($GdCl_3{\cdot}6H_2O$) (Alfa Aesar, USA) or manganese(II) chloride tetrahydrate ($MnCl_2{\cdot}4H_2O$) (Sigma Aldrich, Canada), and deionized water to the final volume. To form homogenous gel structures with the highly cationic gadolinium ions and avoid the crosslinking of the anionic gellan gum, diethylenetriaminepentaacetic acid (DTPA) (Sigma Aldrich, Canada) was used to chelate the gadolinium ions in 2% molar excess. The final gel composition contained 1.25% (w/v) gellan gum, 10% (v/v) propylene glycol for anti-bacterial properties and spatial stability, 7.55 mM methyl 4-hydroxybenzoate as an antiseptic; synthesized SPIONs (0–30 ppm) as T_2 modifiers; $GdCl_3$ (0–140 μM) or $MnCl_2$ (0–40 μM) as T_1 modifiers; DTPA (0–142.8 μM) to stabilize the $GdCl_3$. The gel formulations were poured either into NMR glass tubes (10 mm diameter, 230 mm length) for NMR and MRI measurements or into 4 mL poly(methyl methacrylate) (PMMA) cuvettes for optical scans. Optical scans to study SPION distributions in the gels were performed along the height of PMMA cuvettes using a microplate reader (Infinite 200 Pro, Tecan Group Ltd., Switzerland), equipped with a horizontal cuvette adaptor. Tecan i-control software (Tecan Group Ltd., ver. 1.7.1.12) was used to define a custom plate to take optical readings at 500 nm at thirteen points (1.982 mm apart) along the long axis of the cuvette [28] over a six-week period. As an internal control, fast green FCF dye (Sigma Aldrich, Canada) at 10 μg dye per 1 mg metal salt was added to enable the optical density of each sample to be dependent on the metal salt concentration allowing internal tracking through optical scans.

2.3. Design of experiments and statistical analyses

To obtain tunable relaxation times for various human tissues, designs of experiments were implemented independently for both metal salts to predict the relaxation times of the samples based on the concentration of the contrast agents. A central composite design of experiment was chosen due to its simplicity and ability to determine the quadratic, linear, and interactive effects of the contrast agent concentration on the relaxation properties in the regression model. Initially, each design contained four points at two concentrations of SPIONs and metal salt [29]. The design was augmented with four intermediate points making a central composite design. Furthermore, three centre points in the middle of the design space were used to analyze the variance of prediction and to aid the quadratic effect analysis. In total, 11 compositions were required for the design of experiments with each metal salt. The design order was randomized to ensure consistency. With the data generated, the relaxation times were fitted to the concentration of SPIONs, metal salts, and the interaction between the contrast agents using the statistics program R (version 3.4.3; Vienna, Austria) regression analysis. ANOVA analyses were conducted to determine the significance of the coefficients in the regression models, and the models were refined with only the significant effects [29].

2.4. NMR and MRI measurements

T_1 relaxation times were acquired at low magnetic fields from 230 μT to 1 T on a fast field-cycling NMR relaxometer (SpinMaster

FFC2000 1T C/DC, Stelar, s.r.l., Mede, Italy) by changing the relaxation field in 30 steps, logarithmically distributed using an acquisition field of 380.5 mT. The measurements were conducted at three different temperatures in the relaxometer (20 °C, 25 °C, and 30 °C) to study the effects of temperature on the relaxation properties of each contrast agent in the gel. For higher field strengths, T_1 and T_2 weighted MRI images were acquired in a plane transverse to the cylindrical axis of the NMR tubes (coronal plane of the scanner) for three adjacent 10-mm-thick slices on a 1.5-T GE CVMR and a 3.0-T GE Discovery MR750 clinical scanners (General Electric Healthcare, Milwaukee, WI, USA) at room temperature (25 °C). Any misalignment among the slices was assessed and remedied during image reconstruction using the image registration tools of Matlab (version 9.3, MathWorks, Inc., Natick, MA). In addition, edge and partial-volume effects of the air-glass-gel interface were assessed by eroding the boundaries of the region of interest (ROI) drawn around the gel in each test tube (see Figs. S1 and S2). T_1 measurements were obtained using an Inversion Recovery Fast Spin Echo pulse sequence with 15 inversion times (TI) logarithmically distributed between 50 and 4000 ms. Other imaging parameters include repetition time (TR) = 10 s, Echo time (TE) = 6.5 ms, Echo Train Length (ETL) = 4, slice thickness (THK) = 10 mm, Field of view (FOV) = 130 × 130 mm, matrix size of 256 × 256 points, and receive Bandwidth (BWr) of 125 kHz. T_2 measurements were estimated using a Spin Echo Multi-Echo pulse sequence with 62 different echo times covering a range from 9 ms to 480 ms, TR = 2000 ms, THK = 10 mm, BWr = 83.3 kHz, with a matrix of 256 × 256, FOV = 130 × 130 mm (a representative data set and curve fit is shown in Fig. S3). The signal intensity as a function of inversion time for the stack of images was analyzed on a pixel-by-pixel basis to give the T_1 and T_2 relaxation times of the samples. MATLAB was used to generate non-linear fits for each pixel to mono-exponential equations.

3. Results and discussion

3.1. Particle-size analysis, magnetic properties, and in-gel stability of SPIONs

The prepared SPIONs characterization results are shown in Fig. 1. The TEM image (Fig. 1a) demonstrated that the SPIONs had agglomerated on the TEM sample grid due to electrostatic interactions in the neutral aqueous environment during the drying process. The corresponding particle-size distribution histogram presented in Fig. 1b displayed the average size to be 6.6 nm. A positive skew from a normal distribution indicated the formation of large sized particles. The XRD results confirm the formation of iron oxide particles (Fig. 1c) showing six diffraction rings (peaks) corresponding to the formation of the SPION structure. With the largest diffraction ring, the Scherrer equation (Eq. (1)) estimated the average crystalline size to be 27.5 nm. At this size, the SPIONs are superparamagnetic [30]. The difference in average size estimation between the TEM and XRD may be explained by the positive skew in the histogram indicating the formation of larger particles. The magnetic properties of the synthesized SPIONs are shown in Fig. 1d where the magnetization curve indicated their superparamagnetic nature with minimal hysteresis from the near-zero coercivity and retentivity. The saturation magnetism of 77.24 $A{\cdot}m^2/kg$ (emu/g) is lower than the bulk magnetism of magnetite but is similar to that of other reported SPIONs [30]. The lower saturation magnetism could be accounted for by the large distribution in particle size confirmed by the TEM image and by the production of diamagnetic iron oxide minerals influencing the overall magnetic field. The nonzero retentivity (7.05 $A{\cdot}m^2/kg$ [emu/g]) and coercivity (5.636 mT [56.36 G]) also indicate the non-uniform size distribution of the SPIONs and formation of other iron oxide minerals. However, the concentration of diamagnetic iron structures is expected to be minimal since the XRD diffraction peaks show no indication of other mineral structures.

The distribution of the SPIONs in the gel with or without metal salts was studied by optical scans as shown in Fig. 1e and f. The data indicated an even distribution of the SPIONs with no evidence of settling within the six-week period. The wavelength of 500 nm was chosen to avoid the effect of the FCF dye which does not absorb around 500 nm. Fig. 1e contains the average optical density of the entire cuvette as a solid line to illustrate the SPION distribution around its mean. The SPION distribution optical density profile is not significantly different from the average line, and the variation can be explained by inhomogeneities in the cuvette. Even after six weeks at room temperature, the average optical density did not change significantly. This is further supported by Fig. 1f where the optical density of each composition is not different from the average. Collectively, Fig. 1e and f demonstrate that no change is seen in the spatial stability of the gel over the tested period for any of the compositions.

3.2. Relaxation properties of SPION and metal salts doped gel phantoms

The effect of varying magnetic field strength on the R_1 relaxation rate is plotted in Fig. 2 for different gel compositions. Compared to the base gel (no SPIONs), the concentration of SPIONs (30 ppm and 15 ppm) had no effect on R_1 relaxation rate for all investigated magnetic field strengths (Fig. 1a) suggesting that neither the presence of SPIONs nor their amount influenced the R_1 relaxation rate. However, the R_1 relaxation rates decreased for all the samples as the magnetic field strength increased before reaching a plateau at approximately 0.1 T. This decrease is likely caused by the higher mobility of the water protons in the gelled environment with increased magnetic field. Fig. 2b presented the effect of $MnCl_2$ concentration on the R_1 relaxation rates at a constant SPIONs concentration (30 ppm). At a fixed magnetic field strength, increasing $MnCl_2$ resulted in an increased R_1, as expected. Below 0.05 T, the R_1 profile follows a similar trend for all three samples. Above 0.05 T, $MnCl_2$ increased the relaxation rate greatly before reaching a maximum around 0.5 T, indicating that the gellan gum phantom material with $MnCl_2$ exhibited noticeable differences in relaxation rate when scanned at different magnetic field strengths. Fig. 2c revealed that while $GdCl_3$ increased R_1 in a concentration-dependent manner, its effect did not pass through minimum and maximum points. Again, the concentration of SPIONs in the $GdCl_3$ samples was kept constant (30 ppm). Below 0.01 T, the relaxation rate becomes more dependent on magnetic field strength with the relaxation rates increasing more rapidly than those of the base gel.

Fig. 3 presented the metal salt effect on both R_1 and R_2 relaxation rates for different SPION concentrations at clinically relevant magnetic field strengths. The slopes in Fig. 3a–e represent the relaxivity of the metal salt at the indicated field strength and SPION concentration. The R_1 relaxivity of $MnCl_2$ is more strongly dependent on magnetic field strength than on the SPION concentration. The dependency of field strength causes the relaxivity of $MnCl_2$-containing gels to vary considerably, indicating that a unique model at each magnetic field strength is required to have accurate relaxation properties. Fig. 3b shows the R_2 relaxation rate at 1.5 T and 3 T for $MnCl_2$-containing gels. Similar to the R_1 relaxation rate, the R_2 relaxation rate is also dependent on magnetic field strength; however, the dependency is minor compared to the SPIONs concentration effect. Overall, adding SPIONs affected the R_2 relaxation rate while R_1 relaxation rate was unchanged, allowing an independent control of the two relaxation properties. Fig. 3c represents the T_1–T_2 design space map for $MnCl_2$ and SPIONs containing gels at 1.5 T. Each point represents a scanned sample and its corresponding T_1 and T_2 values with a total of nine distinct concentrations. The solid line indicates an iso-metal salt concentration and the dashed line represents iso-SPIONs concentrations. Known tissue relaxation times [2] are superimposed to the design space to illustrate applicable tissues. Tissue relaxation properties plotted include liver, brain, breast, and kidney tissues with soft tissues fitting within the design space for most of the cases.

Shown in Fig. 3d–f are the $GdCl_3$ and SPIONs containing samples at

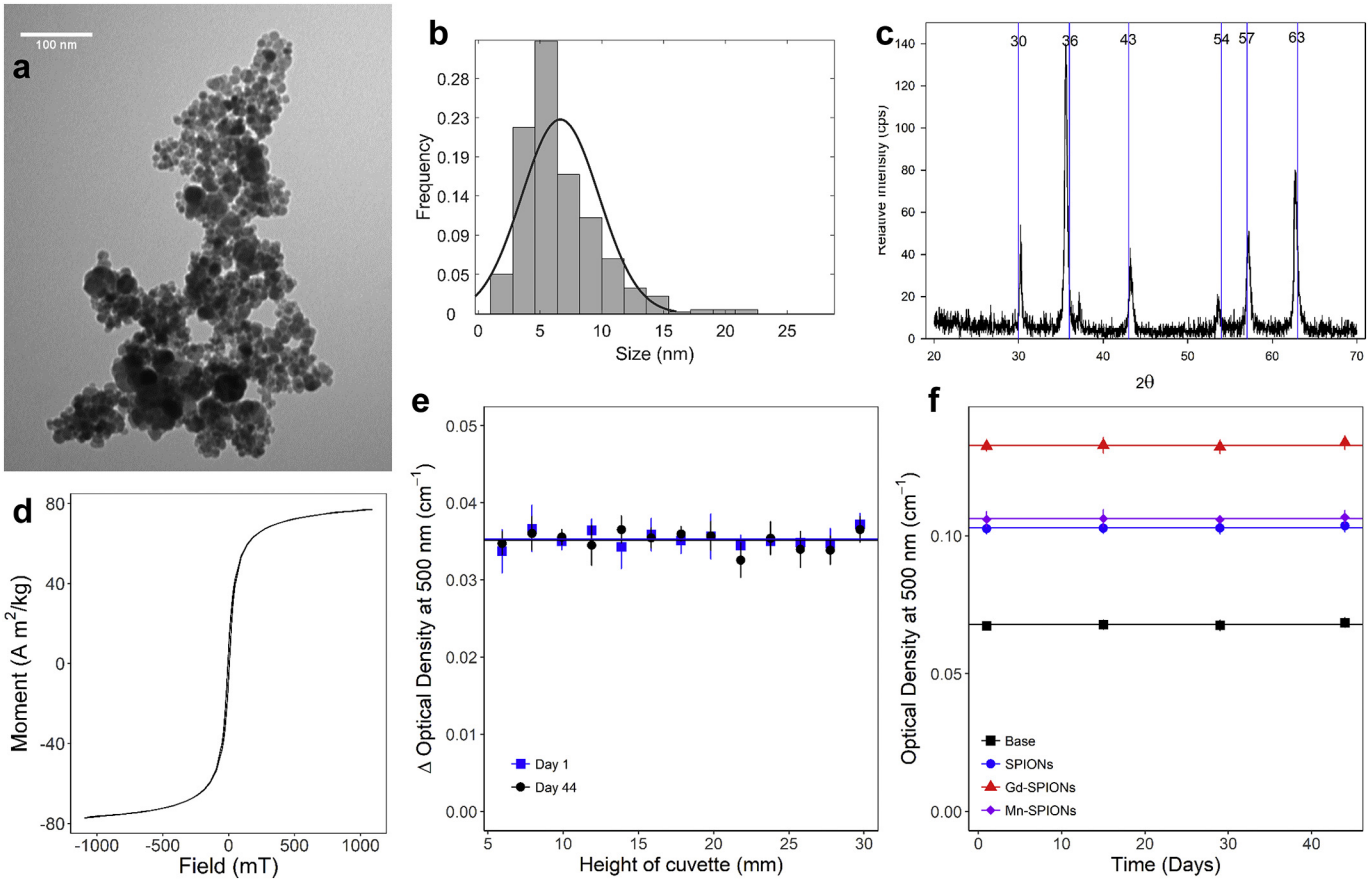

Fig. 1. Characterization of SPIONs. (a) TEM image illustrating the size of the dried SPIONs. (b) Particle size distribution histogram of the TEM images. (c) XRD spectrum of SPION particles. (d) Superparamagnetic properties of SPIONs. (e) Optical scans normalized to the base gel demonstrating distribution of SPIONs in a gel at two time points indicated by "square" for the initial scans and "circle" for 44 days. Done in triplicates and plotted with average value lines. (f) Optical scans for temporal analysis of SPION, SPION-Mn, and SPION-Gd doped gels. The gel compositions were a base gel represented by "square" points, SPIONS by "circle", SPION-$MnCl_2$ by "diamond", and SPION-$GdCl_3$ by "triangle" in triplicates and plotted with average value lines.

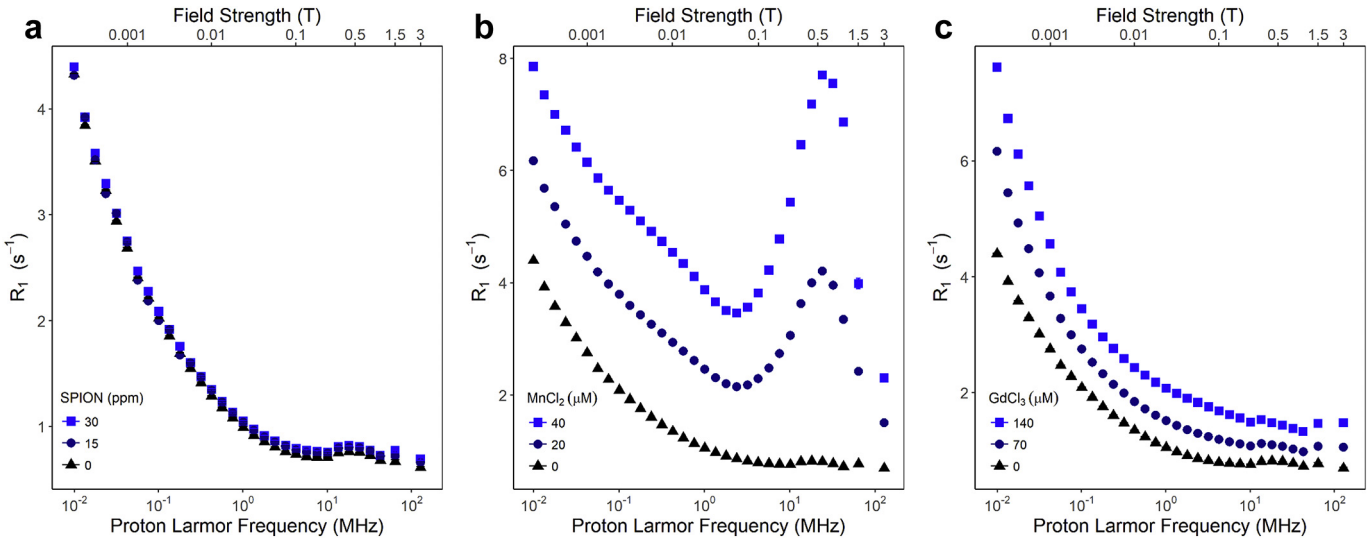

Fig. 2. The effect of magnetic field strength at different concentration of contrast agents on relaxation rates (R_1), log-normal scale. (a) SPIONs, (b) $MnCl_2$ at 30 ppm SPIONs, and (c) $GdCl_3$ at 30 ppm SPIONs. Legend: "square" high concentration of contrast agent, "circle" medium concentration, and "triangle" low concentration.

eight distinct concentrations. Fig. 3d plots the R_1 relaxation rate and the relaxivity of the $GdCl_3$. Both the magnetic field strength and the SPIONs concentrations effects are minor in contrast to the $MnCl_2$ plots where the magnetic field strength was the dominant effect. This result is corroborated in literature which showed stronger dependence on the field strength for the relaxivity induced by manganese-based contrast agents over gadolinium [31]. The R_2 relaxation rates for the $GdCl_3$ samples are plotted in Fig. 3e, and again the metal salt concentration increases the R_2 relaxation rate. The results are comparable to $MnCl_2$ with the SPIONs concentration having a more substantial influence on

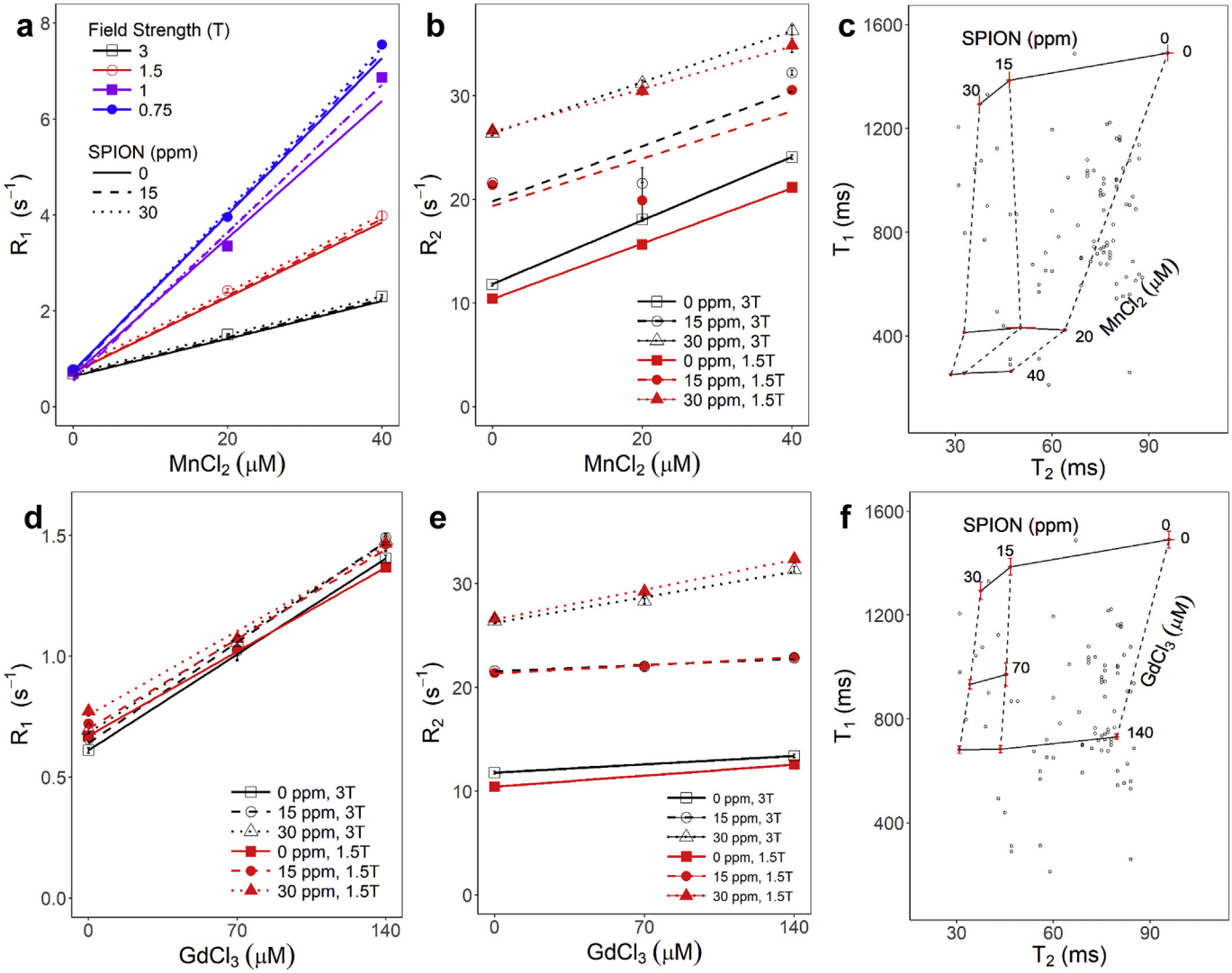

Fig. 3. Relaxivity of the gellan gum gels at varying contrast agent concentrations and magnetic field strengths. (a) R_1 relaxation rate for $MnCl_2$ concentration with the effects of SPION indicated by the line-type ("solid" is 0 ppm, "dashed" is 15 ppm, "dotted" is 30 ppm) and field strength indicated by the colour or the point shape (black "open-square" is 3 T, red "open-circle" is 1.5 T, purple "filled-square" is 1 T, and blue "filled-circle" is 0.75 T. (b) R_2 relaxation rate versus the $MnCl_2$ concentration with the effects of SPION indicated by line-type and by point shape ("solid line and square" is 0 ppm, "dashed line and circle" is 15 ppm, "dotted line and triangle" is 30 ppm) and the field strength is indicated by the colour or point fill (black "open point" is 3 T and red "filled point" is 1.5 T). (c) T_1–T_2 map for $MnCl_2$ at 1.5 T where each "solid" point represents a concentration tested, "solid" lines represent iso-metal salt concertation, and "dashed" lines represent iso-SPION concentration. "open" points represent known relaxation times for various human tissues. Error bars are indicated in red. (d) R_1 relaxation rate versus the $GdCl_3$ concentration with the effects of SPION and the field strength. (e) R_2 relaxation rate versus the $GdCl_3$ concentration with the effects of SPION and the field strength. (f) T_1–T_2 map for $GdCl_3$ at 1.5 T. (For interpretation of the references to colour in this figure legend, the reader is referred to the web version of this article.)

R_2 relaxation rate than magnetic field strength. Samples with no SPIONs have higher R_2 relaxation rates at larger magnetic field strengths (3 T), but when SPIONs are introduced and their concentration is increased a larger relaxation rates is observed at 1.5 T. Therefore, the effect of SPIONs on the R_2 relaxation rate is also dependent on magnetic field strength. Similar to $MnCl_2$, a design space map for $GdCl_3$ samples is plotted at 1.5 T in Fig. 3f with the same known human tissue relaxation times. Strong dependency of the $MnCl_2$-induced relaxivity on the magnetic field strength and temperature has been previously reported [2]; however, the $GdCl_3$-induced relaxivity is less sensitive to field strength and temperature making it more attractive. Nevertheless, $GdCl_3$ has other disadvantages including environmental and health concerns when preparing, handling and disposing [32,33]. Furthermore, the relaxivity induced by $GdCl_3$ is lower than $MnCl_2$ requiring higher concentrations of the metal salt for similar relaxation rates.

3.3. The effect of temperature and time on relaxation properties

To determine the effect of temperature, R_1 relaxation rates were measured at three temperatures (20 °C, 25 °C, and 30 °C) for three gel compositions (40 μM $MnCl_2$, 30 ppm SPIONs + 40 μM $MnCl_2$, and 140 μM $GdCl_3$) as shown in Fig. 4a–c, respectively. The results indicate that temperature does have some effect on the relaxation properties of the gellan gum gel phantom regardless of contrast agent. As the temperature is decreased, the relaxation rates increased slightly, which is a typical response for gel phantoms [34]. Here, this trend was not dependent on the type of contrast agent chosen. As a further analysis of MRI signal stability, a set of samples were re-scanned after six weeks of storage at room temperature. Samples containing the same composition as the temperature study were measured but only the sample containing 30 ppm SPIONs and 40 μM $MnCl_2$ is shown in Fig. 4d as it was hypothesized to change the most with time. All tested composition gave similar results, and after six weeks of storage the R_1 relaxation profile is

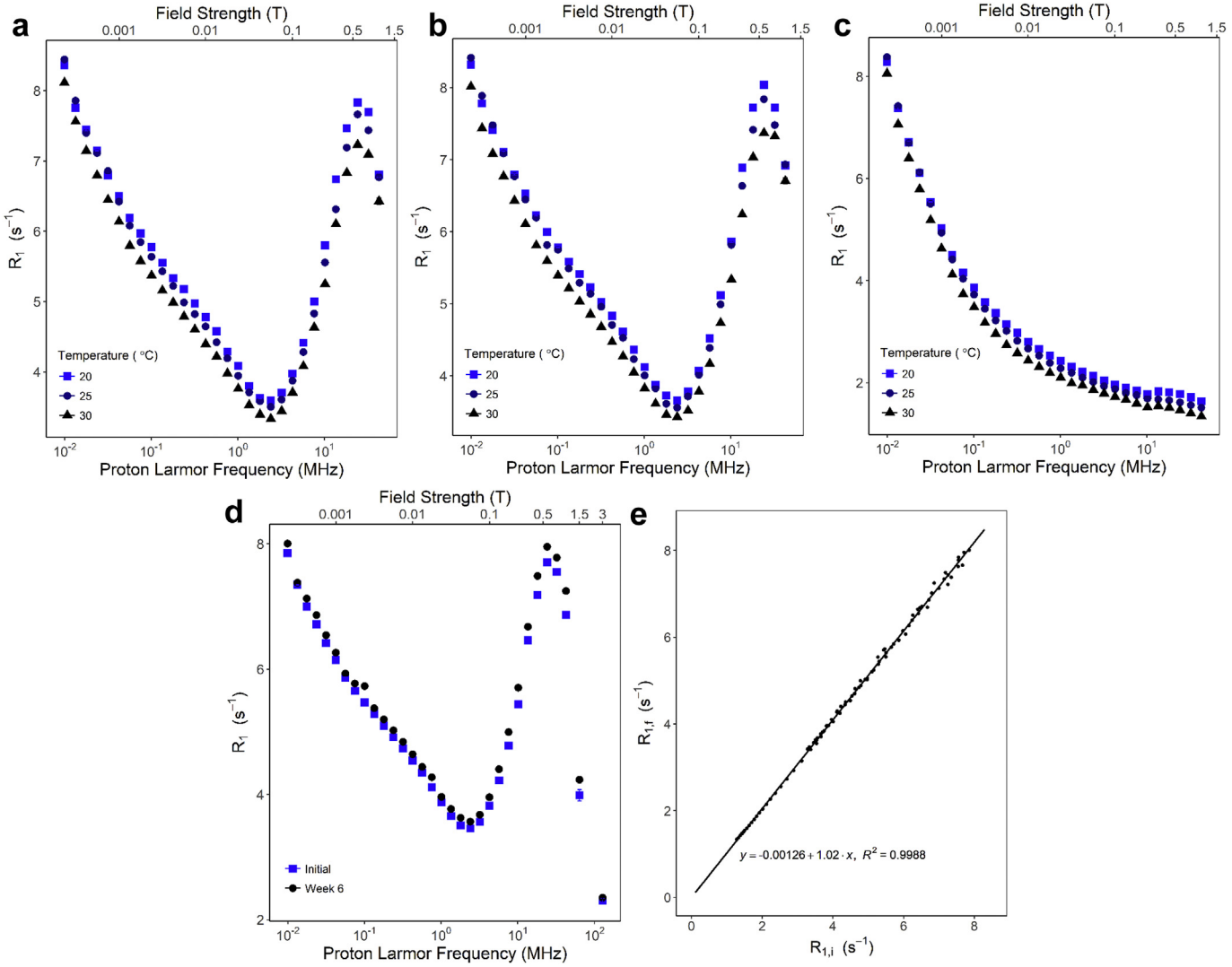

Fig. 4. The effect of temperature on NMR R_1 relaxation rate for gellan gum phantoms. (a) $MnCl_2$, (b) SPION-$MnCl_2$, and (c) $GdCl_3$ as indicated: legend is: "square" for 20 °C, "circle" for 25 °C, and "triangle" for 30 °C). (d) Temporal analysis of R_1 relaxation rate initially "square" and after six weeks "circle". (e) Comparison plot of the initial relaxation rates at initially and after six weeks.

similar, but a slight increase in relaxation rates occurred. Further analysis is shown in Fig. 4e where the relaxation rates at the two time points are compared against each other in a comparison plot where $R_{1,i}$,represents the initial scans and $R_{1,f}$ represents the scans after six weeks. A slight increase in relaxation rates occurs with time shown by the slope of 1.02 instead of 1.00, however, a linear relation exists ($R^2 = 0.9988$) between the results. The increase of relaxation rates may be explained by the loss of water from the gel, which can be prevented by careful sealing.

3.4. Tunable relaxation rates

The central composite design was fitted to the following equation to estimate the base, linear, quadratic, and interaction concentration effects at varying field strengths for a constant temperature of 25 °C.

$$R_i = a_{i,j,0} + a_{i,j,1}\cdot C_{m,j} + a_{i,j,2}\cdot C_S + a_{i,j,3}\cdot {C_{m,j}}^2 + a_{i,j,4}\cdot {C_S}^2 + a_{i,j,5}\cdot C_{m,j}\cdot C_S \quad (2)$$

where R_i represents either longitudinal (R_1; $i = 1$) or transverse (R_2; $i = 2$) relaxation rates; $a_{i,j,k}$ represents the best fit coefficients shown in Tables 1 and 2 with j being 1 for $MnCl_2$ and 2 for $GdCl_3$ and k corresponds to the type of effect (base, linear metal salt, linear SPIONs, quadratic metal salt, quadratic SPIONs, or interactive for 0, 1, 2, 3, 4, or 5 respectively); $C_{m,j}$ is the concentration of metal salt; and C_S is the concentration of SPIONs. Using ANOVA, the significance ($p < 0.05$) of each coefficient to predicting the relaxation rate was evaluated. For R_1, the linear effect of the metal salts was significant at all field strengths. While, the linear SPION effect was significant at 1.5 and 3 T and loses significance at lower field strengths. The quadratic effect of the metal salt was significant between 0.75 and 1 T but loses significance at higher or lower field strengths. The quadratic effects of the SPION concentration and the interaction of the SPION to either metal salt were not significant. With the significance of each parameter known, the linear regression was repeated with the significance terms only. The results can be seen in Table 1a for $MnCl_2$ and Table 2a for $GdCl_3$. The adjusted R^2 values of the linear regressions indicate an excellent fit at all field strengths for $MnCl_2$ (> 0.994) and $GdCl_3$ (> 0.97). Adjusted R^2 value compares the explanatory power of the regression model to the number of parameters used. This way only parameters that are useful in predicting the relaxation rate increase the accuracy of the model. Therefore, the adjusted R^2 values for both metal salts indicated that the model was able of accurately predicting the R_1 relaxation rates within the design space for all magnetic field strength tested. For R_2, the base and linear effects for both metal salts and SPIONs were significant at the

Table 1
Coefficient for relaxation rate equation for $MnCl_2$ at all field strengths tested. (ns) indicate not significant with p-value > 0.05.

(a) Longitudinal relaxation rates (R_1)

Field strength	$a_{1,1,0}$	$a_{1,1,1}$	$a_{1,1,2}$	$a_{1,1,3}$	$a_{1,1,4}$	$a_{1,1,5}$	Adjusted-R^2
	(s^{-1})	$(\mu M{\cdot}s)^{-1}$	$(ppm{\cdot}s)^{-1}$	$(\mu M^{-2}{\cdot}s^{-1})$	$(ppm^{-2}{\cdot}s^{-1})$	$(\mu M{\cdot}ppm{\cdot}s)^{-1}$	
3	0.62 ± 0.02	0.0397 ± 0.0005	0.0028 ± 0.0007	(ns)	(ns)	(ns)	0.998
1.5	0.68 ± 0.03	0.0795 ± 0.0009	0.0038 ± 0.0012	(ns)	(ns)	(ns)	0.998
1.0009	0.71 ± 0.13	0.1116 ± 0.0097	(ns)	0.00097 ± 0.00023	(ns)	(ns)	0.995
0.75691	0.76 ± 0.08	0.1497 ± 0.0062	(ns)	0.00042 ± 0.00015	(ns)	(ns)	0.998
0.56715	0.76 ± 0.04	0.1719 ± 0.0015	(ns)	(ns)	(ns)	(ns)	0.999
0.42505	0.78 ± 0.03	0.1603 ± 0.0012	(ns)	(ns)	(ns)	(ns)	0.999
0.31851	0.79 ± 0.03	0.1399 ± 0.0013	(ns)	(ns)	(ns)	(ns)	0.999
0.23863	0.71 ± 0.04	0.1169 ± 0.0015	(ns)	(ns)	(ns)	(ns)	0.998
0.17885	0.73 ± 0.03	0.0998 ± 0.0011	(ns)	(ns)	(ns)	(ns)	0.998
0.13403	0.73 ± 0.02	0.0868 ± 0.0008	(ns)	(ns)	(ns)	(ns)	0.999
0.10049	0.77 ± 0.02	0.0749 ± 0.0007	(ns)	(ns)	(ns)	(ns)	0.999
0.075277	0.79 ± 0.01	0.0689 ± 0.0006	(ns)	(ns)	(ns)	(ns)	0.999
0.056393	0.84 ± 0.03	0.064 ± 0.0011	(ns)	(ns)	(ns)	(ns)	0.996
0.042268	0.89 ± 0.02	0.0636 ± 0.001	(ns)	(ns)	(ns)	(ns)	0.997
0.031677	0.95 ± 0.02	0.0667 ± 0.0008	(ns)	(ns)	(ns)	(ns)	0.998
0.023729	1.03 ± 0.02	0.0698 ± 0.0008	(ns)	(ns)	(ns)	(ns)	0.998
0.017795	1.12 ± 0.02	0.0732 ± 0.0009	(ns)	(ns)	(ns)	(ns)	0.998
0.013326	1.22 ± 0.03	0.0759 ± 0.0012	(ns)	(ns)	(ns)	(ns)	0.997
0.009985	1.33 ± 0.03	0.0789 ± 0.0012	(ns)	(ns)	(ns)	(ns)	0.997
0.00748	1.46 ± 0.02	0.0807 ± 0.0008	(ns)	(ns)	(ns)	(ns)	0.999
0.0056074	1.59 ± 0.02	0.0817 ± 0.0008	(ns)	(ns)	(ns)	(ns)	0.999
0.0042075	1.72 ± 0.02	0.0838 ± 0.0009	(ns)	(ns)	(ns)	(ns)	0.998
0.0031574	1.9 ± 0.02	0.0833 ± 0.0008	(ns)	(ns)	(ns)	(ns)	0.998
0.0023638	2.06 ± 0.03	0.0846 ± 0.0012	(ns)	(ns)	(ns)	(ns)	0.998
0.0017659	2.25 ± 0.03	0.0841 ± 0.0011	(ns)	(ns)	(ns)	(ns)	0.998
0.0013252	2.38 ± 0.04	0.09 ± 0.0024	0.0025 ± 0.001	−0.00014 ± 0.00006	(ns)	(ns)	0.999
0.00099331	2.75 ± 0.03	0.0837 ± 0.0011	(ns)	(ns)	(ns)	(ns)	0.998
0.00074206	3.01 ± 0.03	0.0839 ± 0.0012	(ns)	(ns)	(ns)	(ns)	0.998
0.00055583	3.27 ± 0.04	0.0854 ± 0.0015	(ns)	(ns)	(ns)	(ns)	0.997
0.00041615	3.57 ± 0.04	0.0851 ± 0.0016	(ns)	(ns)	(ns)	(ns)	0.997
0.00031372	3.85 ± 0.04	0.092 ± 0.0025	0.0034 ± 0.0011	−0.0002 ± 0.00006	(ns)	(ns)	0.999
0.00023315	4.39 ± 0.05	0.0855 ± 0.0022	(ns)	(ns)	(ns)	(ns)	0.994

(b) Transverse relaxation rates (R_2)

Field strength	$a_{2,1,0}$	$a_{2,1,1}$	$a_{2,1,2}$	$a_{2,1,3}$	$a_{2,1,4}$	$a_{2,1,5}$	Adjusted-R^2
	(s^{-1})	$(\mu M{\cdot}s)^{-1}$	$(ppm{\cdot}s)^{-1}$	$(\mu M^{-2}{\cdot}s^{-1})$	$(ppm^{-2}{\cdot}s^{-1})$	$(\mu M{\cdot}ppm{\cdot}s)^{-1}$	
3	12.1 ± 1.5	0.27 ± 0.05	0.44 ± 0.06	(ns)	(ns)	(ns)	0.889
1.5	10.7 ± 1.7	0.23 ± 0.05	0.5 ± 0.07	(ns)	(ns)	(ns)	0.87

field strengths tested. The quadratic concentration effect of the SPIONs was significant with the $GdCl_3$ model while not significant with the $MnCl_2$ model. The quadratic effect of the metal salt and the interaction effect of the SPION to either metal salt were not significant. As with R_1, the linear regressions was repeated accounting for significance terms and are shown in Table 1b for $MnCl_2$ and Table 2b for $GdCl_3$. Again, the adjusted R^2 values indicates a good fit for the $GdCl_3$ model (> 0.978). The adjusted R^2 values for the $MnCl_2$ fit was lower (> 0.87) but still a reasonable fit. With either set of equations, tunable relaxation properties can be targeted and achieved. Even with the 11 and 10 samples for $MnCl_2$ and $GdCl_3$ respectively, the model was accurate showing the benefit of using a design of experiments. The choice of central composite design allowed further analysis into the quadratic effects which were important especially for the R_2 relaxation rates. The design space was limited by the lower limits of relaxation rate of the base gel indicated in Fig. 3c and f, where the gellan gum sample would not be able to model the tissues relaxation properties. This limitation restricts gellan gum samples from mimicking liquids within tissues or tissues with long relaxation times.

3.5. NMRD Relaxivity modeling

The relaxivity dependency to magnetic field strength was plotted on nuclear magnetic relaxation dispersion (NMRD) profiles for each metal salt at 25 °C in the gellan gum gel environment in Fig. 5. The $MnCl_2$-induced relaxivity (Fig. 5a) changes drastically at higher frequencies with a substantial change above 0.01 T; but below 0.01 T, the relaxivity is nearly constant similar to results seen in a pure aqueous environments [35]. The quadratic profile at higher magnetic field strengths was indicative of a large hindrance to the tumbling rate of the bounded hydrogen in the inner sphere [36]. The $GdCl_3$ NMRD is plotted in Fig. 5b and sowing a distinct relaxivitiy profile, compared to $MnCl_2$. A minor effect of field strength exists at the high magnetic field strengths where relaxivity initially decreases before increasing until the relaxivity begins to plateau. However, below 0.02 T the apparent dependency increases resulting in a large relaxivity at lower magnetic field strengths. This profile has been reported for contrast agents used in other gel structures or natural tissue [10,37]; however, the relaxivity in a pure aqueous environment approaches a constant value similar to the $MnCl_2$ profile. This suggest that the gelling structure has an influence on the relaxivity dependency for the $GdCl_3$-containing samples. Potentially the chelated gadolinium ions may still be interacting with the

Table 2
Coefficient for relaxation rate equation for $GdCl_3$ at all field strengths tested. (ns) indicate not significant with p-value > 0.05.

(a) Longitudinal relaxation rates (R_1)

Field strength	$a_{1,2,0}$	$a_{1,2,1}$	$a_{1,2,2}$	$a_{1,2,3}$	$a_{1,2,4}$	$a_{1,2,5}$	Adjusted-R^2
	(s^{-1})	$(\mu M{\cdot}s)^{-1}$	$(ppm{\cdot}s)^{-1}$	$(\mu M^{-2}{\cdot}s^{-1})$	$(ppm^{-2}{\cdot}s^{-1})$	$(\mu M{\cdot}ppm{\cdot}s)^{-1}$	
3	0.61 ± 0.02	0.0057 ± 0.0002	0.0023 ± 0.001	(ns)	(ns)	(ns)	0.99
1.5	0.66 ± 0.03	0.0051 ± 0.0002	0.0029 ± 0.0012	(ns)	(ns)	(ns)	0.98
1.0009	0.71 ± 0.03	0.0031 ± 0.0005	(ns)	0.000009 ± 0.000004	(ns)	(ns)	0.987
0.75691	0.76 ± 0.03	0.0029 ± 0.0006	(ns)	0.000011 ± 0.000004	(ns)	(ns)	0.985
0.56715	0.77 ± 0.02	0.0046 ± 0.0003	(ns)	(ns)	(ns)	(ns)	0.972
0.42505	0.78 ± 0.02	0.0049 ± 0.0003	(ns)	(ns)	(ns)	(ns)	0.975
0.31851	0.77 ± 0.02	0.0053 ± 0.0003	(ns)	(ns)	(ns)	(ns)	0.978
0.23863	0.74 ± 0.03	0.0039 ± 0.0006	(ns)	0.00001 ± 0.000004	(ns)	(ns)	0.988
0.17885	0.73 ± 0.02	0.0057 ± 0.0002	(ns)	(ns)	(ns)	(ns)	0.985
0.13403	0.74 ± 0.02	0.0061 ± 0.0002	(ns)	(ns)	(ns)	(ns)	0.987
0.10049	0.75 ± 0.03	0.0065 ± 0.0003	(ns)	(ns)	(ns)	(ns)	0.982
0.075277	0.79 ± 0.02	0.0068 ± 0.0003	(ns)	(ns)	(ns)	(ns)	0.987
0.056393	0.82 ± 0.02	0.007 ± 0.0003	(ns)	(ns)	(ns)	(ns)	0.988
0.042268	0.89 ± 0.03	0.0059 ± 0.0006	(ns)	0.000009 ± 0.000004	(ns)	(ns)	0.993
0.031677	0.93 ± 0.03	0.0073 ± 0.0003	(ns)	(ns)	(ns)	(ns)	0.986
0.023729	1.01 ± 0.02	0.0074 ± 0.0003	(ns)	(ns)	(ns)	(ns)	0.988
0.017795	1.1 ± 0.03	0.0076 ± 0.0003	(ns)	(ns)	(ns)	(ns)	0.987
0.013326	1.2 ± 0.02	0.0077 ± 0.0003	(ns)	(ns)	(ns)	(ns)	0.988
0.009985	1.31 ± 0.02	0.0079 ± 0.0003	(ns)	(ns)	(ns)	(ns)	0.989
0.00748	1.44 ± 0.02	0.008 ± 0.0003	(ns)	(ns)	(ns)	(ns)	0.99
0.0056074	1.57 ± 0.02	0.0084 ± 0.0003	(ns)	(ns)	(ns)	(ns)	0.991
0.0042075	1.7 ± 0.03	0.0089 ± 0.0003	(ns)	(ns)	(ns)	(ns)	0.989
0.0031574	1.89 ± 0.02	0.0092 ± 0.0003	(ns)	(ns)	(ns)	(ns)	0.993
0.0023638	2.03 ± 0.03	0.0101 ± 0.0003	(ns)	(ns)	(ns)	(ns)	0.991
0.0017659	2.22 ± 0.03	0.0108 ± 0.0003	(ns)	(ns)	(ns)	(ns)	0.991
0.0013252	2.42 ± 0.03	0.0118 ± 0.0003	(ns)	(ns)	(ns)	(ns)	0.994
0.00099331	2.72 ± 0.03	0.0131 ± 0.0003	(ns)	(ns)	(ns)	(ns)	0.995
0.00074206	2.99 ± 0.03	0.0148 ± 0.0004	(ns)	(ns)	(ns)	(ns)	0.994
0.00055583	3.26 ± 0.04	0.0168 ± 0.0004	(ns)	(ns)	(ns)	(ns)	0.994
0.00041615	3.55 ± 0.04	0.0186 ± 0.0004	(ns)	(ns)	(ns)	(ns)	0.995
0.00031372	3.91 ± 0.04	0.0205 ± 0.0005	(ns)	(ns)	(ns)	(ns)	0.995
0.00023315	4.39 ± 0.05	0.0235 ± 0.0005	(ns)	(ns)	(ns)	(ns)	0.995

(b) Transverse relaxation rates (R_2)

Field strength	$a_{2,2,0}$	$a_{2,2,1}$	$a_{2,2,2}$	$a_{2,2,3}$	$a_{2,2,4}$	$a_{2,2,5}$	Adjusted-R^2
	(s^{-1})	$(\mu M{\cdot}s)^{-1}$	$(ppm{\cdot}s)^{-1}$	$(\mu M^{-2}{\cdot}s^{-1})$	$(ppm^{-2}{\cdot}s^{-1})$	$(\mu M{\cdot}ppm{\cdot}s)^{-1}$	
3	11.3 ± 1	0.019 ± 0.005	0.73 ± 0.08	(ns)	−0.0065 ± 0.0025	(ns)	0.978
1.5	9.9 ± 1.1	0.022 ± 0.006	0.82 ± 0.09	(ns)	−0.0073 ± 0.0027	(ns)	0.979

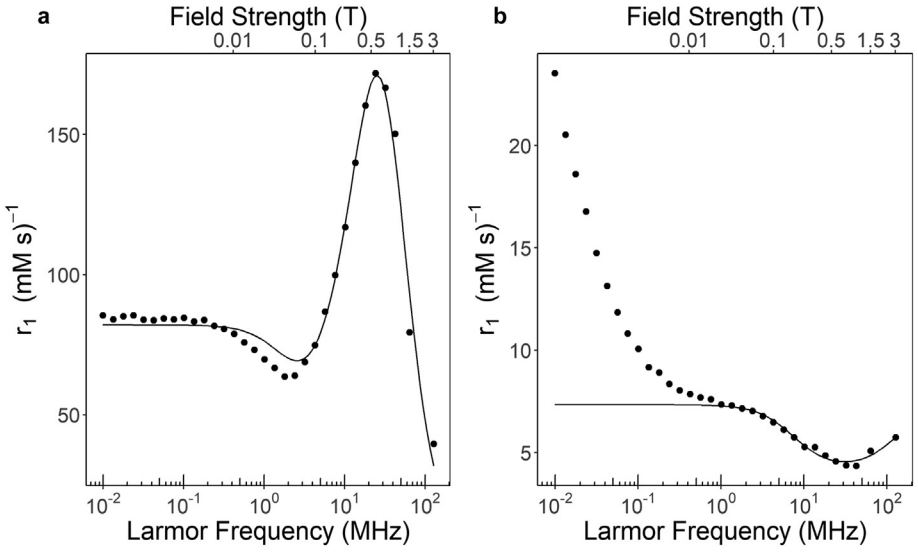

Fig. 5. NMRD profiles modelled by Solomon-Bloembergen-Morgan theory for a) $MnCl_2$ and b) $GdCl_3$. Parameters are reported in Table 3.

Table 3
NMRD best-fit parameters.

Parameter	Description	$MnCl_2$	$GdCl_3$-DTPA
S	Total electron spin	5/2[a]	7/2[a]
q	Number of bound water molecules	1[a]	1[a]
r (nm)	Proton-metal ion distance	2.9[a]	3.13[a]
$A/\hbar$ (10^6 rad/s)	Hyperfine coupling constant	−37.9[a]	−3.9[a]
τ_m (ns)	Water residence time	32.8 ± 5.2	130 ± 40
Δ^2 (10^{19} s^{-2})	Transient ZFS interaction	629 ± 66	2.00 ± 0.46
τ_v (ps)	Fluctuation correlation time	136.1 ± 7.3	8.0 ± 1.4
τ_r (ns)	Rotational correlation time	3000[b]	1.18 ± 0.13

[a] Denotes parameters taken from literature [39–41].
[b] Fixed in the fitting procedure.

gellan gum structure crosslinking the gel and providing a differing relaxation environment. The movement of the hydrogens in the inner sphere near the gadolinium ions would be inhibited causing the profile to differ from aqueous environments and from the $MnCl_2$ profile thus providing a NMRD profile more typically seen in more restricted environments like tissues. Relaxivity of the SPIONs and the quadratic effect of the contrast agents were not shown as their effects were not significant through most of the magnetic field strengths tested.

The NMRD profiles were modelled by the Solomon-Bloembergen-Morgan (SBM) theory which fit a mathematical model to parameters relating to the physical relaxation of the inner sphere hydrogens [36]. Outer sphere relaxation effects were ignored, and focus was placed on the inner sphere relaxation due to the scope of the research and the limits in outer sphere relaxation in complexity and use of more general parameters. The SBM model coefficients are related to the relaxation characteristics of the nearby protons. However, the SBM model is not designed to properly predict low magnetic fields for slowly rotating objects [38], and the gel environment may have caused the protons to rotate slowly. The model was able to approximate the $MnCl_2$ system well as shown in Fig. 5a, but since the $GdCl_3$ sample fails to reach a plateau, the model fails to fit the relaxivity at lower magnetic field strengths (Fig. 5b). This was indicative of slowly rotating protons in the gelled environment with $GdCl_3$ system. Therefore, the $GdCl_3$ was modelled down to 0.02 T to generate the best-fit parameters. Modelled best-fit parameters can be found in Table 3 for both metal salt relaxivity. The values were modelled through nonlinear regression in the statistical program R. Additional studies, which were beyond the scope of this paper, may provide further detail into the relaxation properties of the bound water to metal salts in the gellan gum gel environment and could provide more insight about the best-fit parameters.

4. Conclusions

We developed a gellan gum relaxation MRI phantom with tailorable relaxation properties. The prepared SPIONs MRI relaxivity confirmed the use of an effective T_2 modifier with the potential for further modification with coating and size optimization. A mathematical model was developed that is capable of predicting spin-lattice and spin-spin relaxation properties for a range of concentration of dopants. The model was shown to provide an accurate fit for both R_1 and R_2 relaxation rates. Adjusting the contrast agent concentrations would enable a wide range of tissue equivalent relaxation properties for the gellan gum samples. The effect of temperature on the relaxation rate was found to be minimal. No measurable changes to the appearance of the gel or its optical density profile were observed after six weeks of storage at room temperature demonstrating that methyl 4-hydroxybenzoate and propylene glycol were effective preservatives. A unique model was developed for either $MnCl_2$ or $GdCl_3$ allowing a choice in relaxation modifier. The $MnCl_2$ model was more susceptible to magnetic field variation but requires lower concentrations to reach targeted relaxation times. The $GdCl_3$ model is less dependent on magnetic field variations but is associated with environment and health concerns. A major limitation to the use manganese-based contrast agents is the relaxivity dependency to magnetic field strength. We have offset this limitation by building a unique model at each magnetic field strength allowing the fabrication of magnetic field strength specific material for MRI phantom use. The significant parameters in the relaxation rate regression model were discussed and shown allowing the fabrication of MRI phantoms with predetermined relaxation properties. Finally, the contrast agents relaxivity dependency on magnetic field strength was examined through SBM theory illustrating the effects the gel structure may have on to the proton's magnetic environment.

Acknowledgment

Funding for this work was provided by the Canadian Institutes of Health Research - CHRP Program and the Natural Sciences and Engineering Research Council of Canada (NSERC).

Appendix A. Supplementary data

Supplementary data to this article can be found online at https://doi.org/10.1016/j.mri.2018.10.017.

References

[1] Price RR, Axel L, Morgan T, Newman R, Perman W, Schneiders N, et al. Quality assurance methods and phantoms for magnetic resonance imaging: report of AAPM nuclear magnetic resonance Task Group No. 1. Med Phys 1990;17:287–95.
[2] Kato H, Kuroda M, Yoshimura K, Yoshida A, Hanamoto K, Kawasaki S, et al. Composition of MRI phantom equivalent to human tissues. Med Phys 2005;32:3199–208. https://doi.org/10.1118/1.2047807.
[3] Chen CC, Wan YL, Wai YY, Liu HL. Quality assurance of clinical MRI scanners using ACR MRI phantom: preliminary results. J Digit Imaging 2004;17:279–84. https://doi.org/10.1007/s10278-004-1023-5.
[4] Keenan KE, Ainslie M, Barker AJ, Boss MA, Cecil KM, Charles C, et al. Quantitative magnetic resonance imaging phantoms: a review and the need for a system phantom. Magn Reson Med 2018;79:48–61. https://doi.org/10.1002/mrm.26982.
[5] Gordon MJ, Chu KC, Margaritis A, Martin AJ, Ethier CR, Rutt BK. Measurement of Gd-DTPA diffusion through PVA hydrogel using a novel magnetic resonance imaging method. Biotechnol Bioeng 1999;65:459–67. https://doi.org/10.1002/(SICI)1097-0290(19991120)65:4<459::AID-BIT10>3.0.CO;2-O.
[6] Chu KC, Rutt BK. Polyvinyl alcohol cryogel an ideal phantom material for MR studies of arterial flow and elasticity. Magn Reson Med 1997;37:314–9.
[7] Blechinger JC, Madsen EL, Frank GR. Tissue mimicking gelatin–agar gels for use in magnetic resonance imaging phantoms. Med Phys 1988;15:629–36.
[8] Kamel H, Syms RRA, Kardoulaki EM, Rea M. Surgical wound monitoring by MRI with a metamaterial-based implanted local coil. EPJ Appl Metamater 2018;5:1–7.
[9] Bucciolini M, Ciraolo L, Lehmann B. Simulation of biological tissues by using agar gels at magnetic resonance imaging. Acta Radiol 1989;30:667–9. https://doi.org/10.3109/02841858909174735.
[10] Gossuin Y, Burtea C, Monseux A, Toubeau G, Roch A, Muller RN, et al. Ferritin-induced relaxation in tissues: an in vitro study. J Magn Reson Imaging 2004;20:690–6. https://doi.org/10.1002/jmri.20152.
[11] Mitchell MD, Harold KL, Axel L, Joseph PM. Agarose as a tissue equivalent phantom material for NMR imaging. Magn Reson Imaging 1986;4:263–6.
[12] Christoffersson JO, Olsson LE, Sjöberg S. Nickel-doped agarose gel phantoms in MR imaging. Acta Radiol 1991;32:426–31. https://doi.org/10.1177/028418519103200519.
[13] Yoshimura K, Kato H, Kuroda M, Yoshida A, Hanamoto K, Tanaka A, et al. Development of a tissue-equivalent MRI phantom using carrageenan gel. Magn Reson Med 2003;50:1011–7. https://doi.org/10.1002/mrm.10619.
[14] Ikemoto Y, Takao W, Yoshitomi K, Ohno S, Harimoto T, Kanazawa S, et al. Development of a human-tissue-like phantom for 3.0-T MRI. Med Phys 2011;38:6336–42. https://doi.org/10.1118/1.3656077.
[15] Luca DF, Maraviglia B, Mercurio A. Biological tissue simulation and standard testing material for MRI. Magn Reson Med 1987;4:189–92.
[16] Mazzara PG, Briggs RW, Wu Z, Steinbach BG. Use of a modified polysaccharide gel in developing a realistic breast phantom for MRI. Magn Reson Imaging 1996;14:639–48. https://doi.org/10.1016/j.jemermed.2016.09.002.
[17] Hellerbach A, Schuster V, Jansen A, Sommer J. MRI phantoms - are there alternatives to agar? PLoS One 2013;8. https://doi.org/10.1371/journal.pone.0070343.
[18] Bajaj IB, Survase SA, Saudagar PS, Singhal RS. Gellan gum: fermentative production, downstream processing and applications. Food Technol Biotechnol 2007;45:341–54.
[19] Qiu K, Haghiashtiani G, McAlpine MC. 3D printed organ models for surgical applications. Annu Rev Anal Chem 2018;11. https://doi.org/10.1146/annurev-anchem-061417-125935.

[20] Chen RK, Shih AJ. Multi-modality gellan gum-based tissue-mimicking phantom with targeted mechanical, electrical, and thermal properties. Phys Med Biol 2013;58:5511–25. https://doi.org/10.1088/0031-9155/58/16/5511.
[21] Lorenzo G, Zaritzky N, Califano A. Rheological analysis of emulsion-filled gels based on high acyl gellan gum. Food Hydrocoll 2013;30:672–80. https://doi.org/10.1016/j.foodhyd.2012.08.014.
[22] Cheng B, Chatzinoff Y, Szczepanski D, Bing C, Shaikh S, Wyman O, et al. Remote acoustic sensing as a safety mechanism during exposure of metal implants to alternating magnetic fields. PLoS One 2018;15:e0197380https://doi.org/10.1371/journal.pone.0197380.
[23] Mohammed L, Ragab D, Lin S, Said S, Gomaa H, Mequanint K. Preparation and characterization of glycol chitosan-Fe_3O_4 core–shell magnetic nanoparticles for controlled delivery of progesterone. J Biomater Tissue Eng 2017;7:561–70. https://doi.org/10.1166/jbt.2017.1603.
[24] Penev KI, Wang M, Mequanint K. Tetrazolium salt monomers for gel dosimetry I: principles. J Phys Conf Ser 2017;847. https://doi.org/10.1088/1742-6596/847/1/012048.
[25] Chang S, Lamm SH. Human health effects of sodium azide exposure: a literature review and analysis. Int J Toxicol 2015;22:175–86. https://doi.org/10.1080/10915810390201145.
[26] Andersen AF. Final amended report on the safety assessment of methylparaben, ethylparaben, propylparaben, isopropylparaben, butylparaben, isobutylparaben, and benzylparaben as used in cosmetic products. Int J Toxicol 2008;27(Suppl. 4):1–82. https://doi.org/10.1080/10915810802548359.
[27] Nalawade T, Sogi SP, Bhat K, Bhat K, Sogi SHP, Sogi SHP, et al. Bactericidal activity of propylene glycol, glycerine, polyethylene glycol 400, and polyethylene glycol 1000 against selected microorganisms. J Int Soc Prev Community Dent 2015;5:114. https://doi.org/10.4103/2231-0762.155736.
[28] Penev KI, Mequanint K. Methylthymol blue in Fricke gels. J Phys Conf Ser 2015;573:012030https://doi.org/10.1088/1742-6596/573/1/012030.
[29] Montgomery DC. Design and analysis of experiments. 6 revised ed. New York: John Wiley & Sons; 2007.
[30] Wu W, He Q, Jiang C. Magnetic iron oxide nanoparticles: synthesis and surface functionalization strategies. Nanoscale Res Lett 2008;3:397–415. https://doi.org/10.1007/s11671-008-9174-9.
[31] Villafranca JJ, Yost FJ, Fridovich I. Magnetic resonance studies of manganese and iron (III) superoxide dismutases. J Biol Chem 1974;249:3532–6.
[32] Rabiet M, Brissaud F, Seidel JL, Pistre S, Elbaz-Poulichet F. Positive gadolinium anomalies in wastewater treatment plant effluents and aquatic environment in the Hérault watershed (South France). Chemosphere 2009;75:1057–64. https://doi.org/10.1016/j.chemosphere.2009.01.036.
[33] Gale EM, Atanasova IP, Blasi F, Ay I, Caravan P. A manganese alternative to gadolinium for MRI contrast. J Am Chem Soc 2015;137:15548–57. https://doi.org/10.1021/jacs.5b10748.
[34] Howe FA. Relaxation times in paramagnetically doped agarose gels as a function of temperature and ion concentration. Magn Reson Imaging 1988;6:263–70. https://doi.org/10.1016/0730-725X(88)90400-6.
[35] Aime S, Anelli P, Botta M, Brocchetta M, Canton S, Fedeli F, et al. Relaxometric evaluation of novel manganese(II) complexes for application as contrast agents in magnetic resonance imaging. JBIC J Biol Inorg Chem 2002;7:58–67. https://doi.org/10.1007/s007750100265.
[36] Lauffer RB. Paramagnetic metal complexes as water proton relaxation agents for NMR imaging: theory and design. Chem Rev 1987;87:901–27. https://doi.org/10.1021/cr00081a003.
[37] Araya YT, Martínez-Santiesteban F, Handler WB, Harris CT, Chronik BA, Scholl TJ. Nuclear magnetic relaxation dispersion of murine tissue for development of T1 (R1) dispersion contrast imaging. NMR Biomed 2017;30:e3789https://doi.org/10.1002/nbm.3789.
[38] Ferreira MF, Mousavi B, Ferreira PM, Martins CIO, Helm L, Martins JA, et al. Gold nanoparticles functionalised with stable, fast water exchanging Gd3+ chelates as high relaxivity contrast agents for MRI. Dalton Trans 2012;41:5472–5. https://doi.org/10.1039/c2dt30388d.
[39] Patinec V, Rolla GA, Botta M, Tripier R, Esteban-Gómez D, Platas-Iglesias C. Hyperfine coupling constants on inner-sphere water molecules of a triazacyclononane-based Mn(II) complex and related systems relevant as MRI contrast agents. Inorg Chem 2013;52:11173–84. https://doi.org/10.1021/ic4014366.
[40] Troughton JS, Greenfield MT, Greenwood JM, Dumas S, Wiethoff AJ, Wang J, et al. Synthesis and evaluation of a high relaxivity manganese(II)-based MRI contrast agent. Inorg Chem 2004;43:6313–23. https://doi.org/10.1021/ic049559g.
[41] Merbach A, Helm L, Toth E. The chemistry of contrast agents [in The Chemistry of Contrast Agents in]. John Wiley & Sons; 2013.